

Article

Effect of Periodic Overloads on Short Fatigue Crack Behavior in CuNi₂Si Alloy under Rotating Bending Load

Yahang Qin, Bing Yang *, Bo Feng, Yifan Li, Shoune Xiao, Guangwu Yang  and Tao Zhu

State Key Laboratory of Traction Power, Southwest Jiaotong University, Chengdu 610031, China; yahang_qin@163.com (Y.Q.); 13893277382@163.com (B.F.); yihaifengfan000@163.com (Y.L.); snxiao@swjtu.edu.cn (S.X.); gwyang@swjtu.edu.cn (G.Y.); zhutao034@swjtu.edu.cn (T.Z.)

* Correspondence: yb@swjtu.edu.cn; Tel.: +86-028-86466433

Received: 19 August 2020; Accepted: 17 September 2020; Published: 18 September 2020



Abstract: In this study, the short fatigue crack behavior in a precipitation-strengthened CuNi₂Si alloy was investigated using a replica technique under rotating bending loads with periodic overloads, an overload ratio of 1.5, and the stress ratio of both was $R = -1$. The results show that all the fatigue cracks originated from the surface of the specimen and displayed a trend of slow initiation and then rapid propagation. The introduction of overloads significantly reduced the fatigue crack initiation time and the fatigue life of the sample. The average life of the overloaded samples was only 31% that of the constant load samples. For overload specimens, multiple cracks grew at the same time and merged at different stages, causing the crack length to increase instantaneously after they merged, thereby considerably reducing the fatigue life. Fractographical analysis and observation of the surface-etched sample replica film showed that cracks in samples with and without overload both propagated along the grain boundaries.

Keywords: Cu-Ni-Si alloy; overload; fatigue crack; fatigue fracture

1. Introduction

CuNi₂Si alloy is a precipitation-strengthened copper alloy that exhibits high strength [1,2], good electrical and thermal conductivity [3], and has good resistance to fatigue and corrosion [4]. It is used to manufacture electrical components, such as electrical connectors, circuit breakers, and relays [5,6]. It is also utilized for making the steady clamps in high-speed railway catenary systems [7]. During high-speed train operation, the contact line is momentarily raised and then oscillates while the pantograph sweeps over the catenary, causing the ring to withstand a complex alternating load with impact overload [8] and daily wind load, resulting in the frequent failure of the high-speed rail contact network due to the fatigue failure of the steady clamps, which threatens railway operational safety [9].

There have been several studies on the impact of grain size [10], processing technology [11], and microstructure [10,12–14] on the fatigue properties of the Cu-Ni-Si alloy. In the past two years, researchers conducted a rotating bending fatigue test on a CuNi₂Si alloy with cold working and micro shot peening, under both normal and salty atmospheric conditions. It was found that both the monotonic tensile strength and the yield strength were significantly improved by using the cold-working, which changed the fracture mode under different atmospheric conditions. The micro shot peening formed a fine hardening layer on the surface of the peened specimen and introduced residual compressive stress, therefore delaying the initiation of cracks [7,15]. Besides, Yang et al. investigated the fatigue crack growth behavior of CuNi₂Si alloy under different loading modes and found that the crack of the sample under tensile-compression load propagates approximately an order of magnitude faster than that under rotating bending load. [16]

For studies of overload, Wu [17] and Bai [18] conducted a study on flat specimens with a single overload, while Borrego et al. [19] studied the fatigue crack growth behavior of the thin AlMgSi₁-T6 aluminum alloy sheets under periodic overload conditions, and found that the crack retardation increased with overload periodicity and decreased with stress ratio increases.

In terms of round bar specimens, Dalaei et al. [20] investigated the effect of a single overload on the fatigue durability and residual stress stability of near pearlite steel under shot peening and found that one cycle of overloading could reduce the fatigue life by 25–60% and the introduction of an overload cycle was more detrimental in the tension state than in the compressed state.

Saalfeld et al. [21] analyzed the effect of overloads on the fatigue strength and residual stress stability for tempered and deep-rolled SAE (Society of Automotive Engineers) 1045 steel and found that overloads influenced the near-surface zone negatively, which led to a significant decrease in the fatigue life.

Purnowidodo et al. [22] studied crack growth behavior after an overload on a solid round bar. They found that the retardation or acceleration of growth depended on whether the residual stress state in front of the crack tip was compression or tension.

It can be seen that overload significantly affects the fatigue performance of metal materials. However, there is little research on the short fatigue crack initiation and propagation behavior of CuNi₂Si alloy under periodic overload. Therefore, it is necessary to carry out fatigue crack replica tests of CuNi₂Si alloy specimens under periodic overload conditions to reveal the effect of overload on short crack behaviors.

2. Materials and Tests

2.1. Materials

The test material was derived from CuNi₂Si round bar blanks with main chemical composition of Cu 97.5%, Ni 1.75%, and Si 0.48% (weight %). The material was solution-treated at 850 °C and cold-worked before processing and was further aged at 400 °C for 2 h. The yield strength, the ultimate tensile strength, the elongation, and the Vickers hardness were 583 MPa, 646 MPa, 14.0%, and 202 respectively, and the Vickers hardness was measured by HVS-1000Z micro-hardness tester (Shanghai Lianer, Shanghai, China) with a load of 0.025 kg for 10 s [7].

Using corrosive (10 g FeCl₃ + 30 mL HCl + 120 mL alcohol) to corrode polished samples, Figure 1 shows the metallographic structure of the material. The Y-direction is consistent with the axial direction of the round bar blank. It can be seen that the material is composed of α -Cu with several twins. By using the Olympus OLS4100 confocal laser scanning microscope (OLYMPUS CORP, Tokyo, Japan), it is statically indicated that the average grain sizes of the materials were 56.3 μ m, 90.2 μ m and 55.6 μ m in the X-, Y- and Z-directions, respectively.

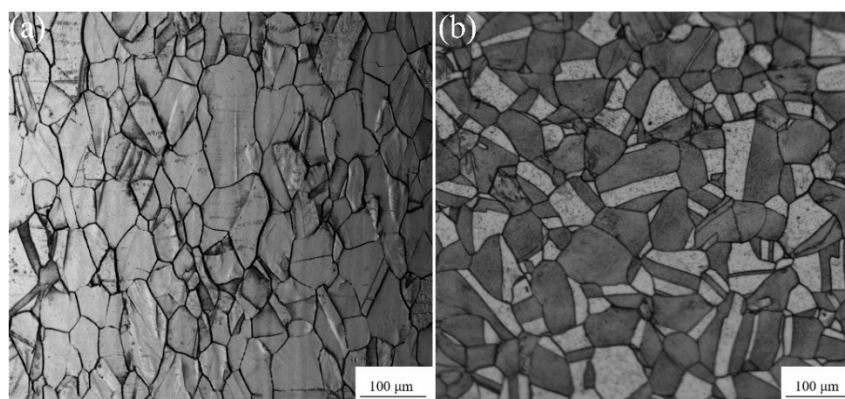


Figure 1. Microstructure of CuNi₂Si alloy obtained by etching: (a) Along longitudinal direction; (b) Along transverse direction.

2.2. Fatigue Tests

The sample shown in Figure 2a was processed. The surfaces of the arc segments of the samples were polished using Al_2O_3 water-soluble suspension with particle sizes of 1 and $0.5\ \mu\text{m}$ to a mirror effect before test. The fatigue tests were performed under a regular room temperature environment using a Horkos RB4-3150 rotating bending fatigue test machine (HORKOS CORP, Hiroshima, Japan) (Figure 2c, $f = 52.5\ \text{Hz}$). The nominal stress levels of the constant load and overload were 240 MPa and 360 MPa (overload ratio of 1.5), respectively, and the stress ratio of both was $R = -1$. The overload time was 10% of the cycle time of each stage. A schematic of the overload is shown in Figure 3, where N_i ($N_1, N_2 \dots$) represents the end of the given overload cycle, at which time the crack growth data were collected.

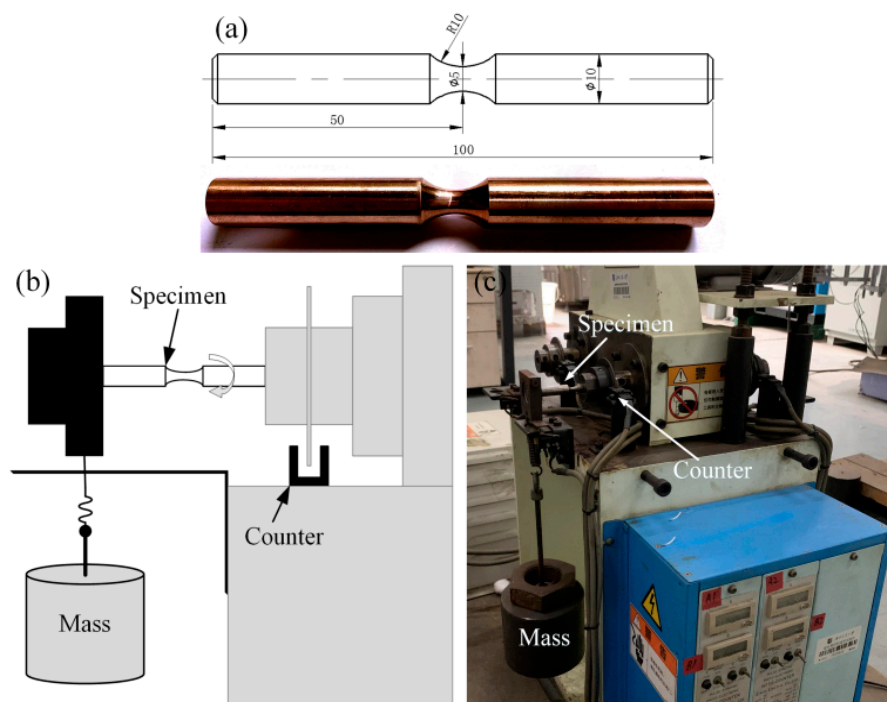


Figure 2. Test equipment: (a) Specimen shape and dimensions (units: mm); (b) Schematic diagram of the fatigue test; (c) Horkos RBE4-3150 rotating bending fatigue test machine.

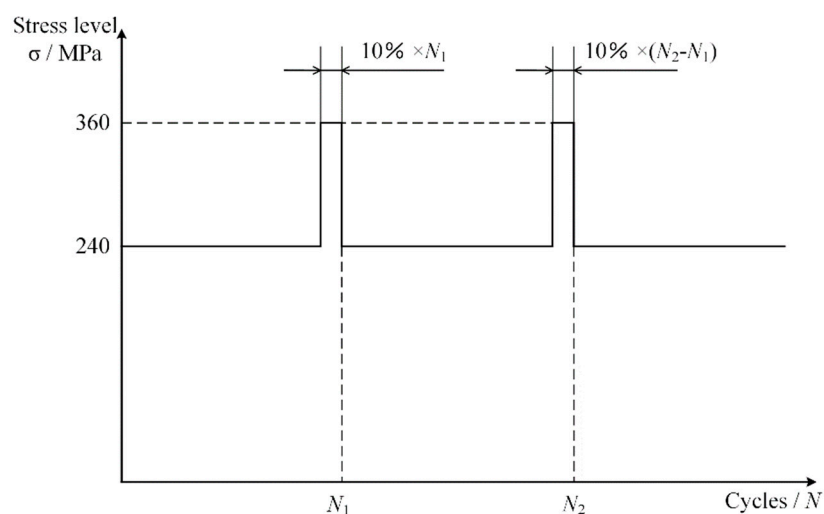


Figure 3. Schematic diagram of overload.

The fatigue crack growth data were obtained using a replica technique [23,24]. The test was interrupted at predetermined cycle numbers to carry out crack replication. The specimen's surface was cleaned with alcohol and a cellulose acetate film was softened with methyl acetate, and then the film was pasted onto the smallest cross-section of the specimen. The films were flattened onto a glass slide when they were completely dry. This process was repeated until the specimen failed. Subsequently, the Olympus OLS4100 laser confocal microscope (OLYMPUS CORP, Tokyo, Japan) was used to capture photographs of the replica films and observe the cracks.

3. Results and Discussion

3.1. Observation of Replica Film

There were four specimens for constant load and four for overload specimens, among which three were smooth surface specimens and one was etched surface specimen. The smooth surfaces of the constant load and overload specimens were numbered CRB1–CRB3 and ORB1–ORB3, respectively. In this preliminary study, a simple average method was used to deal with the life of samples, the fatigue life of each sample and the average life are shown in Table 1.

Table 1. The fatigue life of each specimen.

Specimen Types	Number	Fatigue Life (Cycles)	Average Life (Cycles)
Constant load specimens	CRB1	545,880	790,303
	CRB2	1,416,570	
	CRB3	298,040	
	CRB4 (etched)	900,720	
Overload specimens	ORB1	446,630	248,323
	ORB2	127,380	
	ORB3	240,220	
	ORB4 (etched)	179,060	

Figure 4 shows the photographs of the replica films, which illustrate the crack behavior on the surface of the CRB1 sample. The white box shows the location of crack initiation. The angle between the line, l , connecting the crack tips and the axial direction of the specimen is defined as the crack angle α , and the projection length of the connecting line perpendicular to the axial direction of the specimen is the crack length a , i.e., $a = l \times \sin \alpha$. Cracking initiated at $N = 130,000$ cycles with a length of approximately $27.4 \mu\text{m}$ (Figure 4b), which was smaller than the average grain size. Until $N = 250,000$ cycles, the cracks still propagated relatively slowly, only increasing $31.7 \mu\text{m}$ during the process (Figure 4c). The crack growth rate accelerated between $N = 300,000$ cycles (Figure 4d) and $N = 400,000$ cycles (Figure 4e), and the crack length increased from $323.6 \mu\text{m}$ to $976.5 \mu\text{m}$. By the time of the last replica ($N = 500,000$ cycles), the crack length had increased to $3217.0 \mu\text{m}$ (Figure 4f). The specimen failed after another 40,000 cycles.

The photograph of the last replica film of specimen ORB2 before failure ($N = 100,000$) is shown in Figure 5. Three main cracks can be seen in the picture, designated as Cracks #1–#3, in order. The length of the three cracks were $1393.0 \mu\text{m}$, $1868.1 \mu\text{m}$, and $2885.1 \mu\text{m}$, respectively; the white boxes indicate the locations of crack initiation. The first crack observed was Crack #1, which had an initial length of approximately $23.0 \mu\text{m}$. Subsequently, Crack #2 and Crack #3 initiated at $N = 2000$ cycles and $N = 10,000$ cycles, with initial crack lengths of approximately $12.4 \mu\text{m}$ and $9.8 \mu\text{m}$, respectively. To clarify different crack sources and cracks that existed due to multiple crack initiations and merges during the crack initiation and propagation of a single specimen, the symbol “i-Cj” was applied to depict the crack originated from the jth crack source of the ith crack. For example, “1-C2” indicates the crack originated from the second crack source of the first crack.

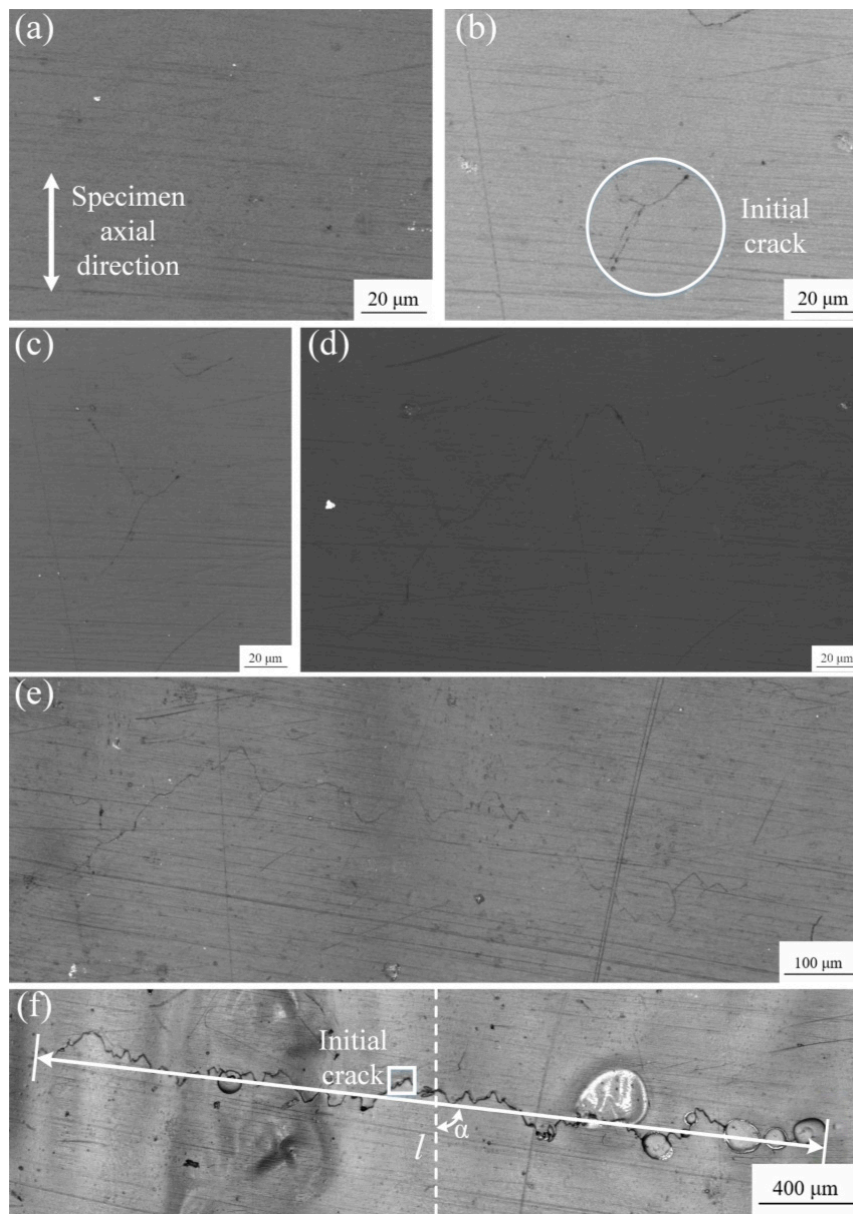


Figure 4. Replica film photos for specimen CRB1 after different numbers of cycles: (a) $N = 0$; (b) $N = 130,000$; (c) $N = 250,000$; (d) $N = 300,000$; (e) $N = 400,000$; (f) $N = 500,000$.

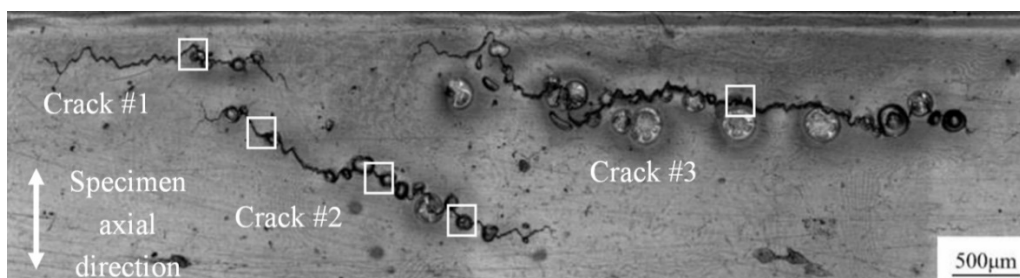


Figure 5. Crack locations and crack sources of specimen ORB2.

Taking Crack #1, the earliest initiated crack, as an example, Figure 6 shows the typical stages during crack propagation.

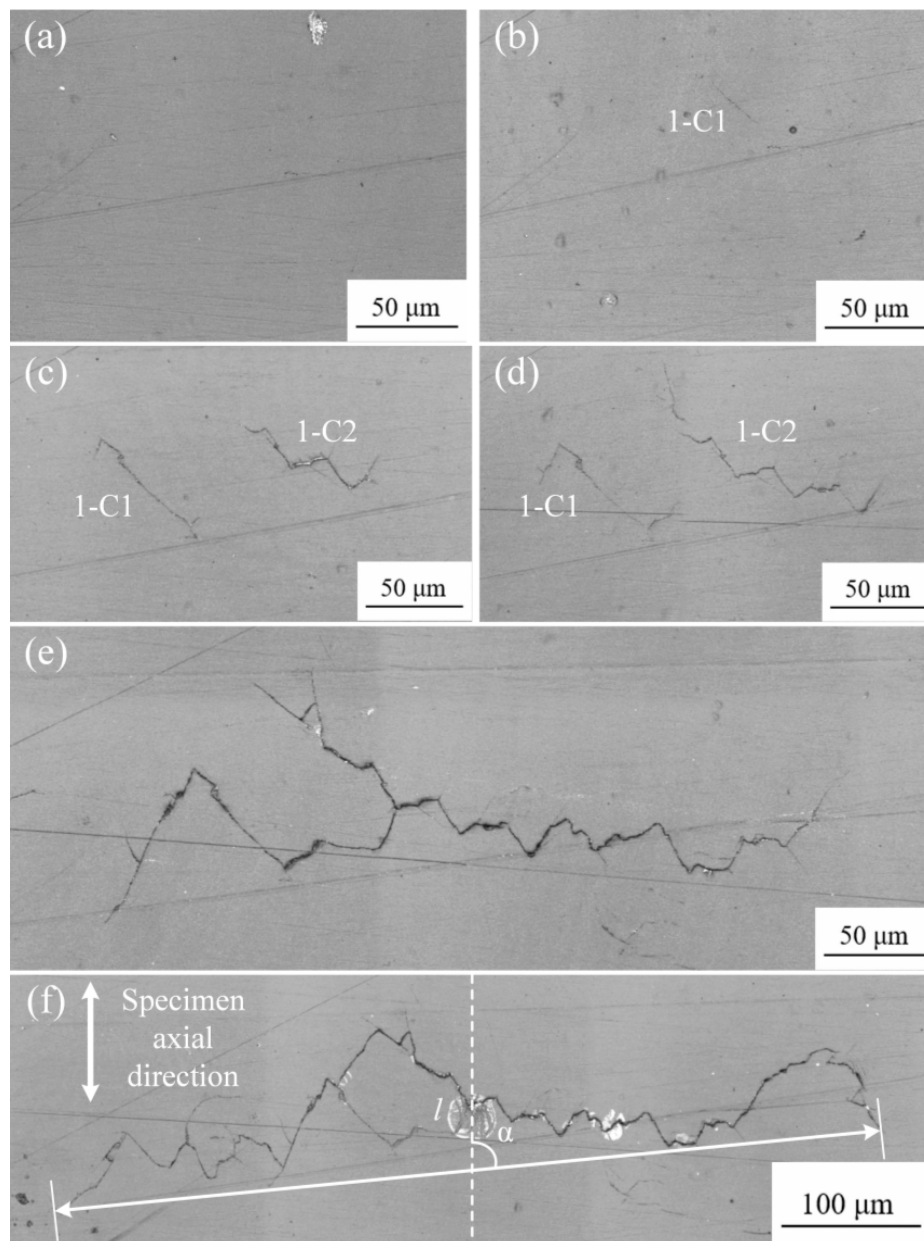


Figure 6. Replica photos of the typical stages for specimen ORB2-Crack #1: (a) $N = 0$; (b) $N = 1000$; (c) $N = 10,000$; (d) $N = 20,000$; (e) $N = 50,000$; (f) $N = 80,000$.

Table 2 shows the length of each crack of specimen ORB2 at different cycles. Crack #1 initiated at $N = 1000$ cycles (Figure 6b); while there was no crack at the same location at $N = 0$ cycle, slight scratches caused by processing were present (Figure 6a). Crack 1-C2 can be observed at $N = 10,000$ cycles (Figure 6c), Cracks 1-C1 and 1-C2 propagated individually during $N = 10,000$ cycles and $N = 50,000$ cycles, and the growth rate of 1-C2 was faster than 1-C1. The two cracks merged at $N = 50,000$ cycles and continued to propagate until the specimen failed. Crack #2 was initiated after Crack #1, and Cracks 2-C2 and 2-C3 were observed at $N = 10,000$ and $N = 20,000$ cycles with initial lengths of 17.1 μm and 15.8 μm , respectively. All three cracks propagated separately until Crack 2-C2 and 2-C3 merged at $N = 80,000$ cycles and then merged with 2-C1 at $N = 100,000$ cycles. Crack #3 initiated last; Crack 3-C1 was observed at $N = 50,000$ cycles with an initial length of 55.3 μm and merged with crack 3-C2 at $N = 80,000$ cycles until fracture.

Table 2. Crack lengths of specimen ORB2 (unit: μm).

Cycles N	Life Fraction f	#1		#2			#3	
		1-C1	1-C2	2-C1	2-C2	2-C3	3-C1	3-C2
1000	0.0079	23.0	-	-	-	-	-	-
2000	0.0157	31.2	-	12.4	-	-	-	-
5000	0.0393	37.9	-	24.7	-	-	-	-
10,000	0.0785	57.0	72.2	51.0	-	15.8	-	9.8
20,000	0.1570	75.8	122.7	101.2	17.1	74.1	-	20.4
50,000	0.3925	363.4		174.3	146.1	159.3	55.3	55.3
80,000	0.6280	667.5		299.6		858.7		779.1
100,000	0.7851	1393.0			1868.1			2885.1

3.2. Observation of Fracture

A scanning electron microscope was used to observe the fractures of the samples, and the fracture photos of the constant load and overload samples are depicted in Figures 7 and 8, respectively. Figures b–d are partially enlarged views taken at the points indicated as b, c, and d in Figure a, respectively. The fatigue fracture for both constant load and overload is composed of three zones, that is, the initiation zone, stable growth zone, and final fracture zone. All the cracks initiated from the surface of the specimen. In the stable propagation zone, several intergranular facets can be observed, which indicates that the cracks mainly propagated along the grain boundaries. In Figures 7d and 8d, tiny dimples and secondary cracks are obvious in the transient fracture zone.

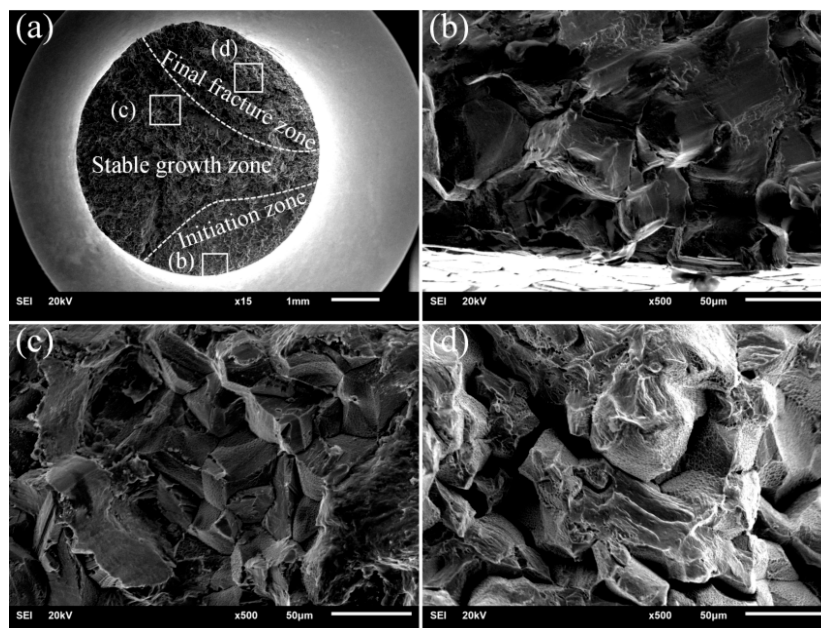


Figure 7. Fracture observations of a constant load specimen: (a) Overview of the fracture; (b) Crack initiation zone; (c) Crack stable growth zone; (d) Final fracture zone.

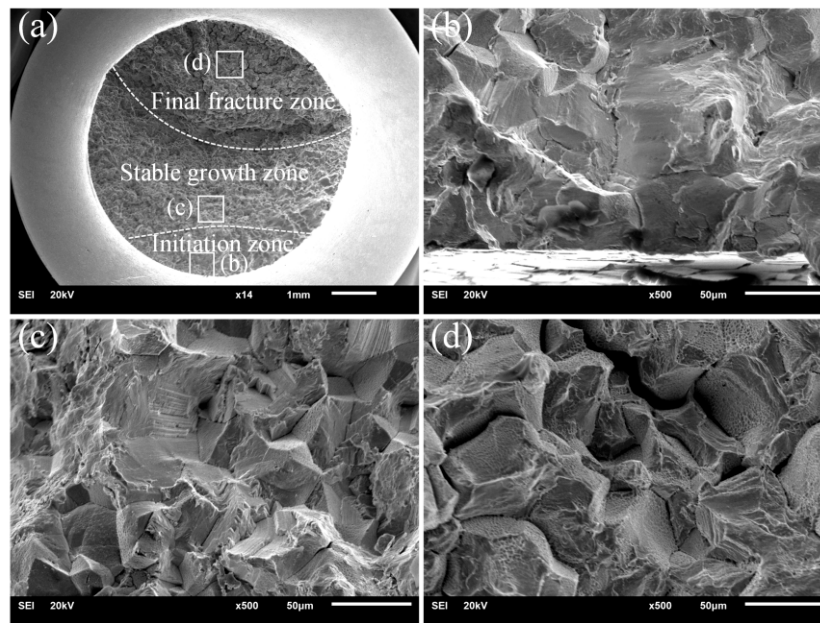


Figure 8. Fracture observations of an overload specimen: (a) Overview of the fracture; (b) Crack initiation zone; (c) Crack stable growth zone; (d) Final fracture zone.

3.3. Crack Propagation Behaviors

Based on the crack lengths measured from the replica films, curves of the crack lengths of the typical constant load specimens CRB1 to CRB3 and overload specimens ORB1 to ORB3 were plotted as a function of the fatigue life fraction, as illustrated in Figure 9.

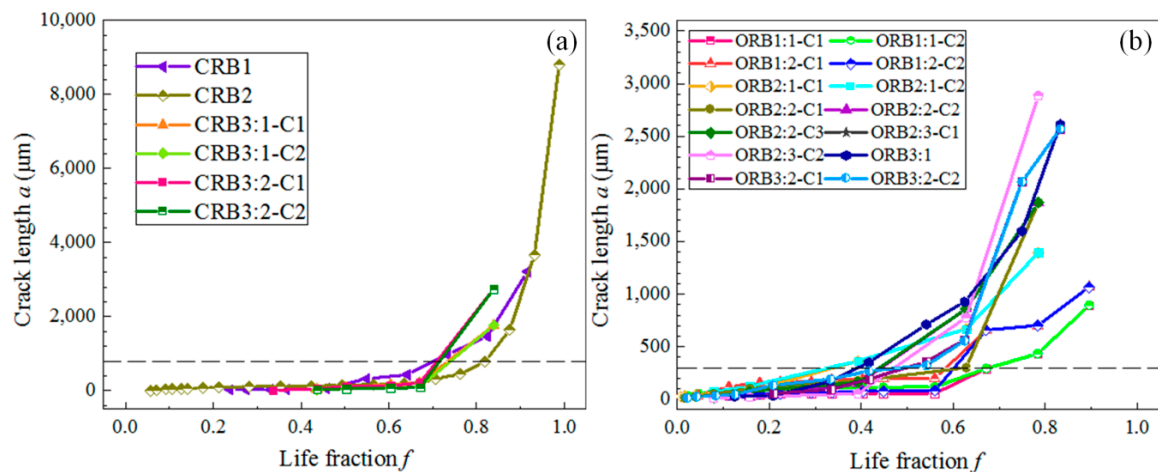


Figure 9. The curves of crack length as a function of life fraction: (a) Constant load; (b) Overload.

It can be seen from Figure 9 that the crack growth was slow for constant load specimens before a life fraction of 0.8. For overload specimens, there were multiple cracks, and the cracks propagated slowly before a life fraction of 0.4. When the life fraction was between 0.4 and 0.6, the cracks accelerated, with different cracks merging. When the life fraction was about 0.6, several cracks merged into one main crack, resulting in a large increase in crack length. For both the constant load and overload specimens, there was a turning point at which the crack changed from slowly increasing to rapidly expanding. The crack length corresponding to this moment is defined as the critical crack size, and from Figure 9, the critical crack sizes for constant load and overload specimens were approximately 800 μm and 300 μm , respectively.

Representative samples of the constant load and overload samples were selected, and the curves of the crack growth rates as functions of the life fractions were plotted as shown in Figure 10. The crack growth rate was calculated using the five-point method [25]. For the convenience of comparison and explanation, Figure 11 separately presents the curves of the crack lengths of these two samples as a function of life fraction.

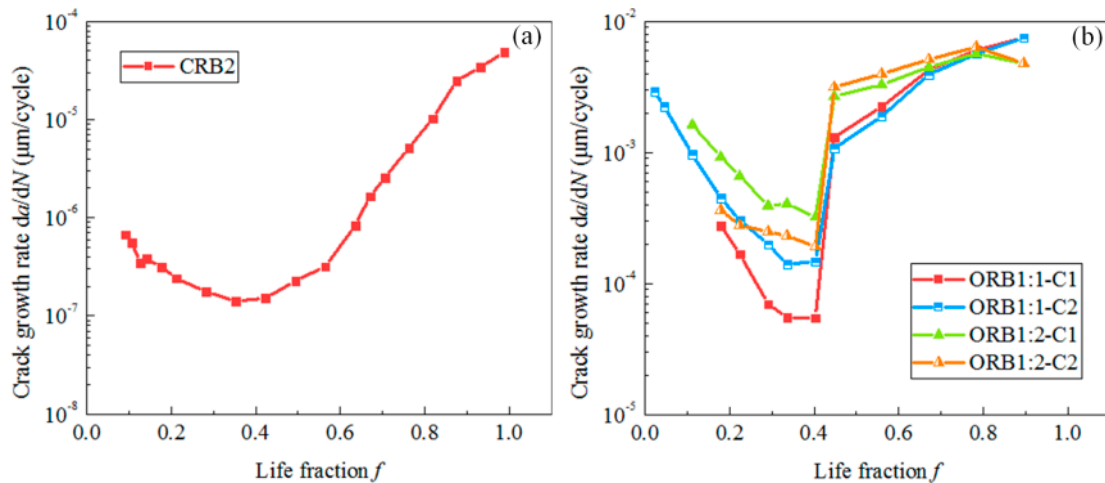


Figure 10. Curves showing crack growth rate as a function of life fraction: (a) CRB2; (b) ORB1.

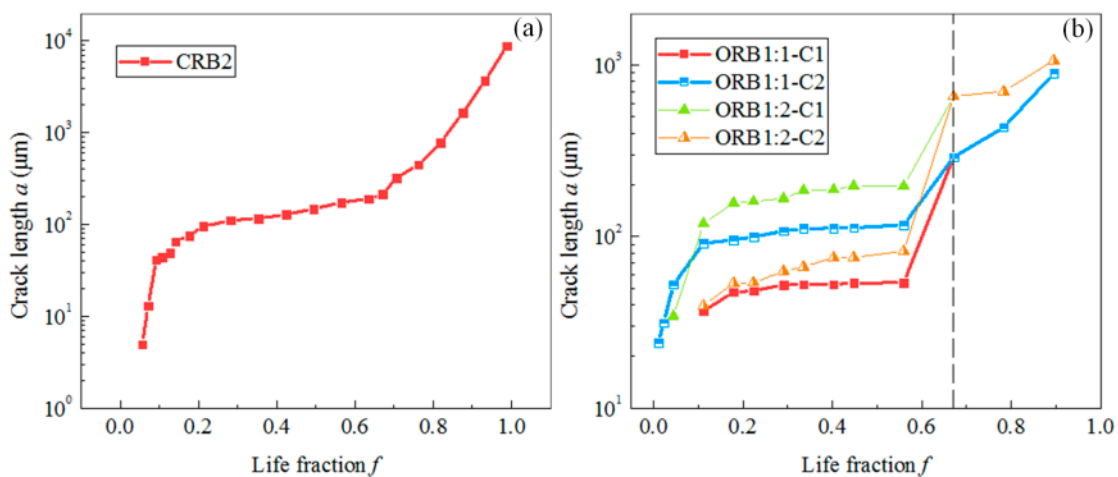


Figure 11. Curves showing crack length as a function of life fraction: (a) CRB2; (b) ORB1.

It can be observed from Figures 10 and 11 that both the constant load and overload samples had crack growth in the early stage of crack initiation, and the growth rate was relatively high within a grain-size range, but then the crack growth rate decreased. This may be because the plastic zone at the crack tip had a dislocation accumulation at the grain boundary before it was transmitted to the next grain, and it required greater plastic deformation to break through the grain boundary [26]. Further, because of the existence of high-angle grain boundaries, short cracks must accumulate more driving force due to the greater difference in the orientation of the active slip system between grains when crossing the adjacent grain boundaries [27].

The five-point method for calculating the crack growth rate at a certain time requires two crack length data points before and after that time. From Figure 11b, it can be seen that when the life fraction of the sample ORB1 was 0.67, two cracks that originated from two crack sources each merged, and the crack length increased significantly, resulting in a sudden increase in the crack growth rate as compared to the previous observation at a life fraction of 0.45. In general, the crack growth rate of the overload samples was greater than that of the constant load samples.

Figures 12 and 13 show the side view of the fracture for the etched specimens under constant load and overload, respectively, together with the corresponding photographs of the replica films before testing and near fracture. It can be found that the cracks in both the constant load and overload specimens mainly propagated along the grain boundaries; however, because the metallographic structure was exposed after the sample was etched, the grain boundaries and cracks cannot be effectively distinguished during the crack initiation and propagation stages. The cracks can only be observed on the replica film near the fracture.

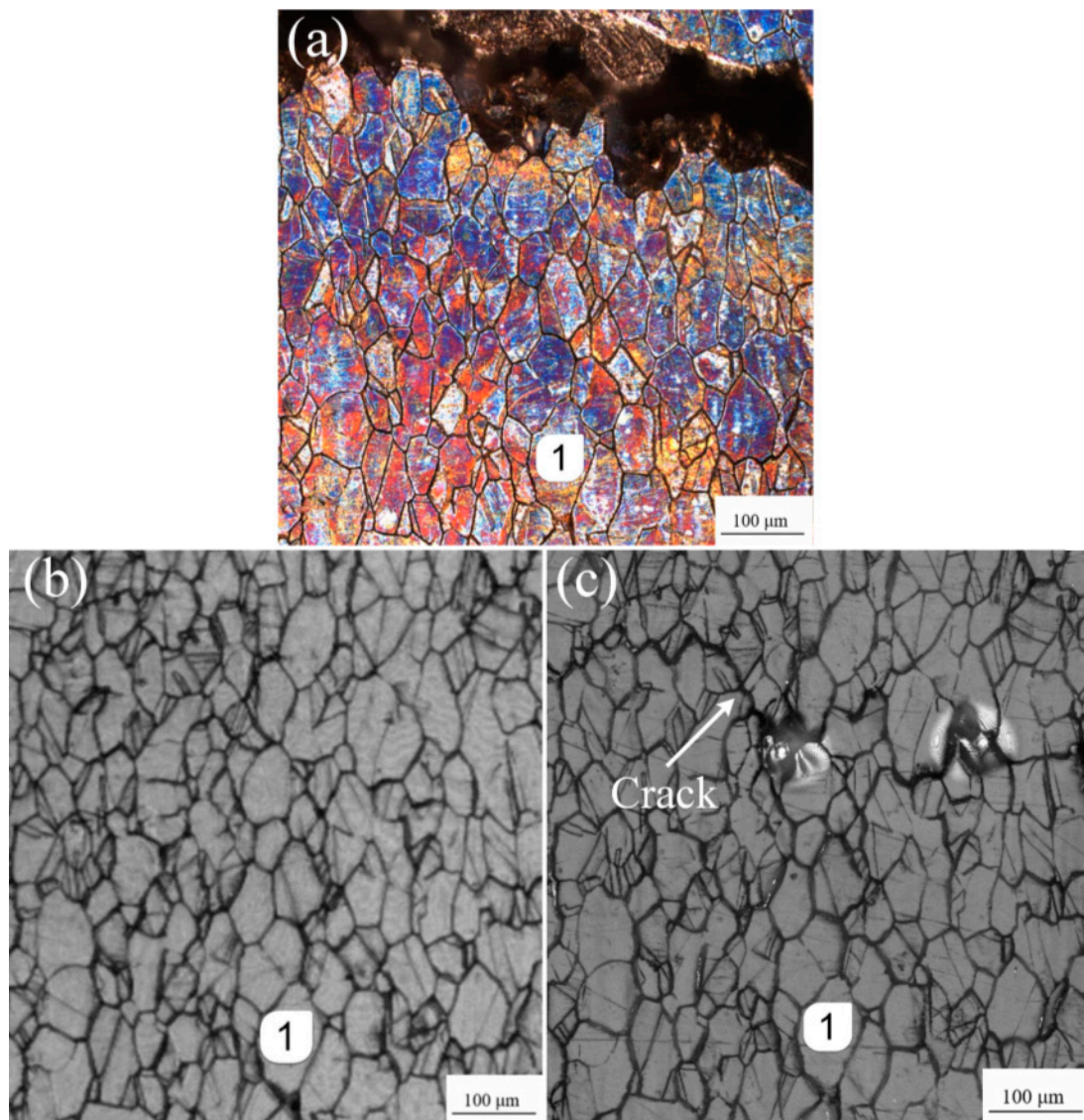


Figure 12. Side view of the fracture and corresponding replica film (etched constant load specimen): (a) the fracture side view of the etched surface specimen; (b) the photograph of the replica films before testing; (c) the photograph of the replica films near the fracture.

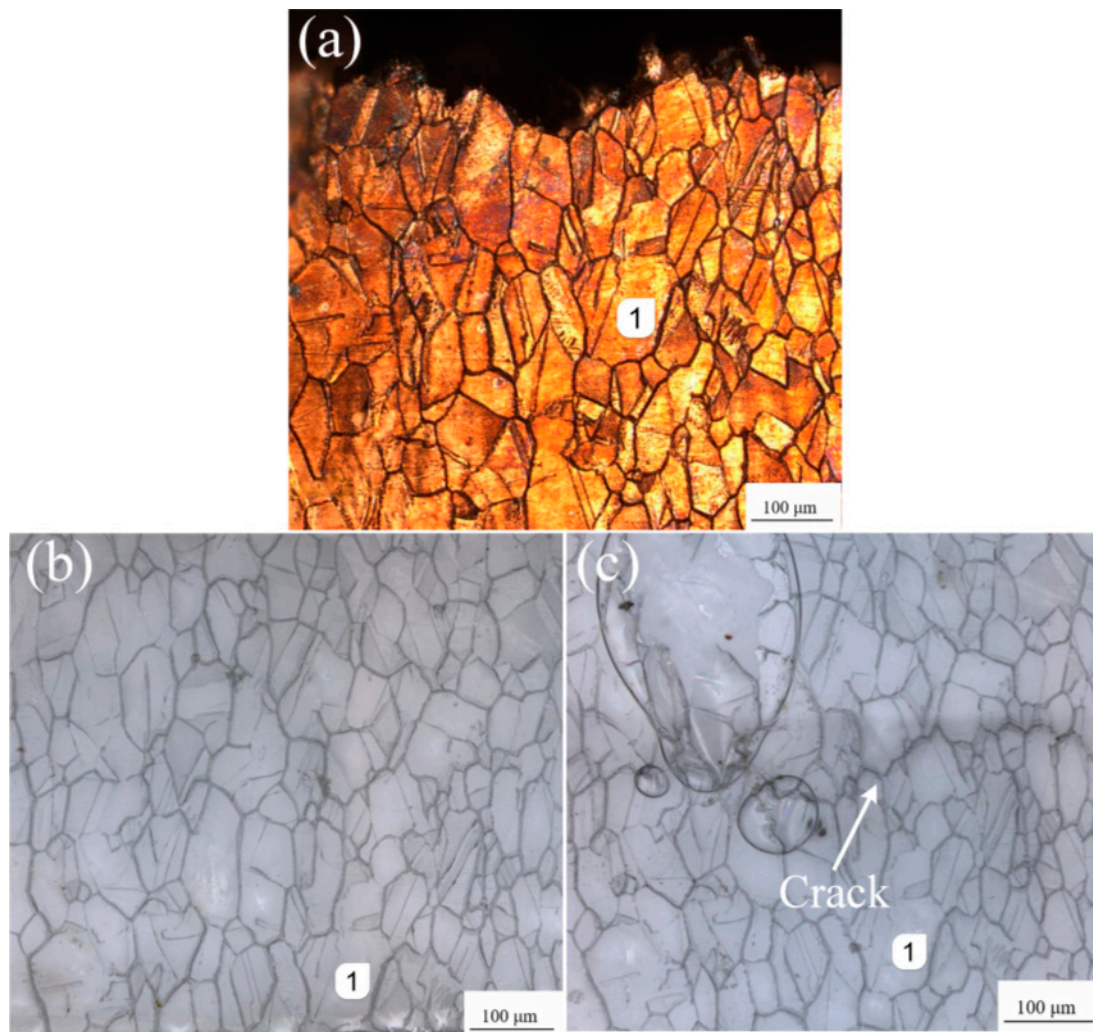


Figure 13. Side view of fracture and corresponding replica film (etched overload specimen): (a) the fracture side view of the etched surface specimen; (b) the photograph of the replica films before testing; (c) the photograph of the replica films near fracture.

3.4. Discussion

Short fatigue cracks mainly originated in the slip bands or grain boundaries. Under a cyclic load, a persistent slip band is generated in the direction of the maximum shear stress. Due to the continuous accumulation of dislocations, the interface between the slip band and the crystal matrix separates, forming a slip band crack. Grain boundary cracks occur primarily because the dislocation accumulation in the high-angle grain boundaries is greater than in the interior of the grains, resulting in crack initiation at the grain boundaries [26]. Observation of the sample fracture shows that, under cyclic loading, cracks nucleated at twins or high-angle grains. Dislocations accumulate at the grain boundaries through slip deformation, causing the initiation of fatigue cracks. The replica film observations of the etched samples show that the cracks mainly propagated along the grain boundaries.

The existence of overload has a certain effect on crack initiation. For constant load specimens, both single-crack and multi-crack initiation existed while all the overloaded specimens exhibited multi-crack initiation. Additionally, the crack initiation times of the three overload specimens occurred at 5000, 1000, and 5000 cycles, while the crack initiation time of the constant load specimens was later than that of the overload specimens, at 130,000, 80,000, and 100,000 cycles. The average life of the constant load specimens in the test was 790,000 cycles, whereas that of the overload specimens was 250,000 cycles or 31% of the constant load specimen life. The difference between the two can be explained in terms

of the number of cracks that simultaneously initiated on the surface of the specimen. For overload specimens, multiple cracks grew at the same time and merged at different stages, causing the crack length to increase instantaneously after they merged, thereby considerably reducing the fatigue life.

It can be seen from the observation of the replica films that the crack grew in a zigzag pattern in the direction perpendicular to the axial direction of the sample; this is related to the inherent characteristics of the grains that prevent dislocation slipping. The crack length increases slowly at first and then expands rapidly with increasing life fraction. The crack sizes of the constant load and the overload samples corresponding to their critical moments were approximately 800 μm and 300 μm , respectively.

4. Conclusions

(1) For all the specimens, cracks originated from the surface through slip deformation. All the overload specimens exhibited multiple cracks initiating from multi-crack sources, while the constant load specimens displayed both single and multi-crack initiation and had a much later crack initiation time.

(2) The existence of overload greatly reduced the fatigue life of the sample. The average life of the overload specimens was 250,000 cycles, which is significantly lower than the 790,000 cycles of the constant load specimens. Compared with the constant load specimens, the slow propagation stage of the overload specimens only accounted for 40% of their lifespan, whereas that of the constant load specimens was 80%. The crack sizes of the constant load and the overload specimens corresponding to the critical moment at which cracks started to rapidly expand after slowly increasing were approximately 800 μm and 300 μm , respectively.

(3) For both the constant load and overload specimens, the cracks generally propagated along the grain boundaries, indicating an intergranular fracture mode.

Author Contributions: The author' contributions are as follows: B.Y. was in charge of the whole trial; Y.Q. wrote the manuscript and guided the numerical simulations; B.F. and Y.L. assisted with sampling and laboratory analyses; S.X., G.Y. and T.Z. guided the experiments. All authors have read and agreed to the published version of the manuscript.

Funding: This research was funded by National Natural Science Foundation of China, Grant/Award Numbers: 51675446, U1534209; Independent Subject of State Key Laboratory of Traction Power, Grant/Award Numbers: 2019TPL-T13.

Acknowledgments: The authors sincerely thank Bing Yang and Shoune Xiao of Southwest Jiaotong University for his critical discussion and reading during manuscript preparation.

Conflicts of Interest: The authors declare no conflict of interest.

References

1. Lei, Q.; Li, Z.; Wang, J.; Xie, J.; Chen, X.; Li, S.; Gao, Y.; Li, L. Hot working behavior of a super high strength Cu–Ni–Si alloy. *Mater. Des.* **2013**, *51*, 1104–1109. [[CrossRef](#)]
2. Lei, Q.; Xiao, Z.; Hu, W.; Derby, B.; Li, Z. Phase transformation behaviors and properties of a high strength Cu–Ni–Si alloy. *Mater. Sci. Eng. A* **2017**, *697*, 37–47. [[CrossRef](#)]
3. Jia, L.; Lin, X.; Xie, H.; Lu, Z.L.; Wang, X. Abnormal improvement on electrical conductivity of Cu–Ni–Si alloys resulting from semi-solid isothermal treatment. *Mater. Lett.* **2012**, *77*, 107–109. [[CrossRef](#)]
4. Lei, Q.; Li, Z.; Han, L.; Xiao, Z.; Xiao, T. Effect of Aging Time on the Corrosion Behavior of a Cu–Ni–Si Alloy in 3.5 wt% NaCl Solution. *Corrosion* **2016**, *72*, 615–627. [[CrossRef](#)]
5. Wang, H.Q.; Wu, M.Z.; Zhang, J.W.; Lu, L.T. On the effect of precooling deformation on fatigue performance and failure behavior of Cu–Ni–Si alloy. *J. Exp. Mech.* **2018**, *33*, 877–884.
6. Huang, F.; Ma, J.; Ning, H.; Cao, Y.; Geng, Z. Precipitation in Cu–Ni–Si–Zn alloy for lead frame. *Mater. Lett.* **2003**, *57*, 2135–2139. [[CrossRef](#)]
7. Yang, B.; Wu, M.; Li, X.; Zhang, J.; Wang, H. Effects of cold working and corrosion on fatigue properties and fracture behaviors of precipitate strengthened Cu–Ni–Si alloy. *Int. J. Fatigue* **2018**, *116*, 118–127. [[CrossRef](#)]
8. Hui, Z.; Xiaohui, X.; Guangfeng, Q.; Hongyan, X.; Hongmei, L. Analysis of fatigue life of catenary dropper for high-speed railway. *Eng. J. Wuhan Univ.* **2019**, *4*, 11.

9. Zhao, G.H. Analysis on Problems Existed on Integral Droppers of Overhead Contact System for High Speed Railway and Their Counter-measures. *Electr. Railw.* **2017**, *28*, 14–18.
10. Gholami, M.; Veselý, J.; Altenberger, I.; Kuhn, H.A.; Wollmann, M.; Janecek, M.; Wagner, L. Influence of grain size and precipitation hardening on high cycle fatigue performance of CuNiSi alloys. *Mater. Sci. Eng. A* **2017**, *684*, 524–533. [[CrossRef](#)]
11. Goto, M.; Iwamura, T.; Han, S.Z.; Kim, S.; Yamamoto, T.; Lim, S.; Ahn, J.H.; Kitamura, J.; Lee, J. Fatigue crack initiation and propagation behaviors of solution-treated and air-cooled Cu-6Ni-1.5Si alloy strengthened by precipitation hardening. *Int. J. Fatigue* **2019**, *123*, 135–143. [[CrossRef](#)]
12. Goto, M.; Han, S.Z.; Lim, S.; Kitamura, J.; Fujimura, T.; Ahn, J.H.; Yamamoto, T.; Kim, S.; Lee, J. Role of microstructure on initiation and propagation of fatigue cracks in precipitate strengthened Cu–Ni–Si alloy. *Int. J. Fatigue* **2016**, *87*, 15–21. [[CrossRef](#)]
13. Gholami, M.; Veselý, J.; Altenberger, I.; Kuhn, H.A.; Janecek, M.; Wollmann, M.; Wagner, L.; Kermanshahi, M.G. Effects of microstructure on mechanical properties of CuNiSi alloys. *J. Alloys Compd.* **2017**, *696*, 201–212. [[CrossRef](#)]
14. Goto, M.; Yamamoto, T.; Han, S.Z.; Lim, S.; Kim, S.; Iwamura, T.; Kitamura, J.; Ahn, J.H.; Yakushiji, T.; Lee, J. Microstructure-dependent fatigue behavior of aged Cu-6Ni-1.5Si alloy with discontinuous/cellular precipitates. *Mater. Sci. Eng. A* **2019**, *747*, 63–72. [[CrossRef](#)]
15. Zhang, J.; Li, X.; Yang, B.; Wang, H.; Zhang, J. Effect of micro-shot peening on fatigue properties of precipitate strengthened Cu-Ni-Si alloy in air and in salt atmosphere. *Surf. Coat. Technol.* **2019**, *359*, 16–23. [[CrossRef](#)]
16. Yang, B.; Li, Y.; Qin, Y.; Zhang, J.; Feng, B.; Liao, Z.; Xiao, S.; Yang, G.; Zhu, T. Fatigue Crack Growth Behaviour of Precipitate-Strengthened CuNi₂Si Alloy under Different Loading Modes. *Materials* **2020**, *13*, 2228. [[CrossRef](#)]
17. Wu, Y.; Bao, R. Fatigue crack tip strain evolution and crack growth prediction under single overload in laser melting deposited Ti-6.5Al-3.5Mo-1.5Zr-0.3Si titanium alloy. *Int. J. Fatigue* **2018**, *116*, 462–472. [[CrossRef](#)]
18. Bai, S.; Sha, Y.; Zhang, J. The effect of compression loading on fatigue crack propagation after a single tensile overload at negative stress ratios. *Int. J. Fatigue* **2018**, *110*, 162–171. [[CrossRef](#)]
19. Borrego, L.F.; Costa, J.M.; Ferreira, J.M. Fatigue crack growth in thin aluminium alloy sheets under loading sequences with periodic overloads. *Thin Walled Struct.* **2005**, *43*, 772–788. [[CrossRef](#)]
20. Dalaei, K.; Karlsson, B. Influence of overloading on fatigue durability and stability of residual stresses in shot peened normalized steel. *Mater. Sci. Eng. A* **2011**, *528*, 7323–7330. [[CrossRef](#)]
21. Saalfeld, S.; Scholtes, B.; Niendorf, T. On the influence of overloads on the fatigue performance of deep rolled steel SAE 1045. *Int. J. Fatigue* **2019**, *126*, 221–230. [[CrossRef](#)]
22. Purnowidodo, A.; Makabe, C. The crack growth behavior after overloading on rotating bending fatigue. *Eng. Fail. Anal.* **2009**, *16*, 2245–2254. [[CrossRef](#)]
23. Yang, B.; Zhao, Y. Experimental research on dominant effective short fatigue crack behavior for railway LZ50 axle steel. *Int. J. Fatigue* **2012**, *35*, 71–78. [[CrossRef](#)]
24. Jordon, J.; Bernard, J.; Newman, J.C. Quantifying microstructurally small fatigue crack growth in an aluminum alloy using a silicon-rubber replica method. *Int. J. Fatigue* **2012**, *36*, 206–210. [[CrossRef](#)]
25. Jia, F.Y.; Huo, L.X.; Zhang, Y.F.; Jing, H.Y.; Yang, X.Q.; Wang, D.P. Comparison with two data processing methods on fatigue crack growth rate. *J. Mech. Strength* **2003**, *25*, 568–571.
26. Hansson, P. Crack growth rates for short fatigue cracks simulated using a discrete dislocation technique. *Int. J. Fatigue* **2009**, *31*, 1346–1355. [[CrossRef](#)]
27. Christina, B.; Solveig, M. Growth of a short fatigue crack—A long term simulation using a dislocation technique. *Int. J. Solids Struct.* **2009**, *46*, 1196–1204.

